Nuclear envelope budding is a non-canonical mechanism to export large transcripts in muscle cells

Sofia Zaganelli[1], Janet B Meehl[1], Robert G Abrisch[1], Gia K Voeltz[1,2].

[1] Department of Molecular, Cellular & Developmental Biology, University of Colorado Boulder, Boulder, CO 80309, USA

[2] Lead contact

SUMMARY

The nuclear pore complex (NPC) is considered the sole route to transport molecules across the nuclear envelope (NE). In recent years, NE budding (NEB) has emerged as an alternative route for nuclear export of viral particles that are too large to pass through the NPC. Yet, the significance of this unconventional export pathway for large endogenous cargoes in mammalian cells has remained largely unexplored. Here, we use a combination of electron and fluorescence microscopy to demonstrate that NEB events occur coincidently with the differentiation of myoblasts into myotubes and concomitant with the expression of uniquely long muscle-specific transcripts. We show that NE buds are derived from the inner nuclear membrane, contain internal vesicles, and they are specifically enriched with long sarcomeric transcripts. Moreover, we demonstrate the role for an RNA-binding protein and membrane remodeling factors in mRNA targeting to NE buds and NE bud biogenesis. Our findings uncover with mechanistic insight a non-canonical pathway for large transcript packaging and export in muscles cells.

INTRODUCTION

In eukaryotic cells, the nuclear envelope (NE) provides a double-membraned barrier, confining the cell genome within the nucleus. The NE is composed of an inner and an outer nuclear membrane (INM and ONM, respectively), characterized by distinct protein compositions [1,2]. The nuclear pore complex (NPC) has long been considered the sole gateway between the nucleus and the cytoplasm, allowing the transport of molecules across the NE [3,4]. However, the size of the NPC channel, approximately 60 nm in diameter when fully stretched [5], limits the passage of macromolecular complexes larger than that diameter. Based on the current export model, very large ribonucleoparticles (RNPs) would need to undergo structural remodeling and partial disassembly for export through the NPC. An alternative possibility is that large RNP cargoes exit the nucleus via a non-canonical pathway that does not require their disassembly. Precedent for such a mechanism exists during the replication cycle of DNA viruses, such Herpesviruses[6]. The newly formed viral nucleocapsid is assembled in the nucleus as a very large macromolecular complex and has been shown to egress from the nucleus by budding across the NE[7,8]. Herpesvirus nuclear egress uses a combination of host and viral proteins to: (1) locally phosphorylate and disassemble the nuclear lamina to expose the INM; (2) build a nuclear egress complex (NEC) for capsid envelopment at the INM and membrane curvature; (3) bud off the capsid-containing vesicle in the space between INM and ONM, known as perinuclear space (PNS) (a process known as primary envelopment); and finally (4) fuse the enveloped capsids with the ONM to release them into the cytosol (a process called de-envelopment). We hypothesized that the NEB pathway is a non-canonical route that mammalian cells normally use to export large macromolecules out of the nucleus, and viruses have co-opted this pathway for their own egress.

A handful of recent studies have begun to investigate the physiological role of NEB at the molecular level, even though NE buds (also reported in literature as herniations) have been observed in electron micrographs of non-infected mammalian cells since the 1950s [9–15]. Several roles have now been ascribed to NEB, ranging from NPC turnover to nuclear quality control [16–25].

In addition, ground-breaking work from Budnik and colleagues proposed that NEB is involved in the export of large RNP (megaRNPs) at the Drosophila neuromuscular junction (NMJ), with a mechanism sharing several similarities with the more characterized process of Herpesvirus nuclear egress [26]. Nevertheless, NEB remains an underexplored potential nuclear transport route for endogenous RNA export in mammalian cells. Here, we show that NEB is a non-canonical pathway to export uniquely long sarcomeric transcripts during myogenesis using a murine cell model. We identify three machineries that work sequentially in this pathway: 1) an RNA-binding protein UIF that targets long mRNA cargoes into NEBs for export; 2) the membrane remodeling ESCRT-III (endosomal sorting complex required transport III) machinery, which is involved in membrane scission of vesicles containing cargoes from the INM similar to its role in nuclear egress [27]; and 3) CLCC1 (chloride channel CLIC-like protein 1), which prior evidence [28] and our findings here indicate is involved in the process of fusion of cargo-containing vesicles with the ONM.

RESULTS

Nuclear envelope buds appear during myogenesis

Given the size constraints associated with nuclear pore export, we hypothesized that exceptionally large endogenous transcripts could represent ideal cargo for NEB-mediated mRNA nuclear export. The longest transcript found in mammalian cells is Titin, which is over 100,000 nucleotides long in its mature form and encodes the third most abundant protein found in muscle cells. During differentiation into muscle (myogenesis), mononucleated myoblasts fuse with each other to generate post-mitotic syncytia (myotubes), which will later develop into mature myofibers. This process involves the assembly of sarcomeres—the contractile units of muscle cells—and, importantly, results in the expression of several of the largest proteins and transcripts in mammalian cells, including Titin, Nebulin, Obscurin, and Dystrophin. Thus, we focused our work on muscle differentiation using C2C12 murine myoblasts, a well-established *in vitro* model of myogenesis, ideally suited for investigating the nuclear export of extremely large mRNAs. We analyzed both C2C12 myoblasts (prior to differentiation, in which myogenic markers and Titin are not expressed), and differentiated myotubes (after 6 days of differentiation, in which both myogenic markers and long sarcomeric transcripts are highly expressed) (**Figure 1A**).

To investigate the presence of NE buds during myogenesis, we used transmission electron microscopy (TEM), which allowed us to visualize the NE and distinguish the INM from the ONM. C2C12 myoblasts were grown on sapphire disks and cultured for 6 days in differentiation medium to promote myotube formation. Undifferentiated myoblasts or differentiated myotubes were high-pressure frozen to ensure optimal membrane preservation. Undifferentiated myoblasts display a canonical NE morphology, with both INM and ONM distinguishable, as well as several NPCs along the NE (**Figure 1B**). In contrast, differentiated myotube nuclei exhibit obvious NE buds in the majority of nuclear volumes examined (**Figure 1C**). From sequential thin sections totaling approximately 200 nm, we observed NE buds in 69.2% of these myotube nuclei sections compared to only 2.7% in myoblast nuclei (**Figure 1C-E**). Multiple NE buds are frequently found in a single nucleus. Further analysis revealed that most of NE buds are single-membrane structures that protrude into the nucleoplasm (**Figure 1C-D**). The average diameter of these NE buds analyzed by TEM is about 350 nm, with some as large as 1 µm (**Figure 1F**). We excluded from our analysis double-membrane structures, which may represent NE invaginations, as well as smaller structures found in the PNS that resemble the NE buds previously linked to NPC biogenesis or quality control defects [18,19,21,29]. A defining feature of NE buds is that the vast majority (81.3%) contain multiple internal luminal vesicles (ILVs), often showing electron dense inclusions, and we define these structures here as Type I NE buds (**Figure 1G-H**). The average

diameter of ILVs found within NE buds is about 173 nm (**Figure 1I**). Electron tomography revealed smaller ILVs within NE buds, as well as omega-shaped nascent ILVs undergoing inward budding towards the lumen of the bud (**Figure 1J and K**). Together, these data demonstrate that NE buds in murine myotubes consist of a single lipid bilayer, protrude into the nucleoplasm, and typically contain multiple ILVs.

NE buds are derived from the INM

We performed immunofluorescence and high-resolution fluorescence microscopy experiments to determine whether NE buds originate from the INM or the ONM. We visualized the INM and ONM using antibodies against endogenous markers specific to each membrane (**Figure 2A**). These experiments demonstrated that NE buds can be visualized in C2C12-derived myotubes by immunostaining against INM-residing proteins (Emerin, LEMD2, LBR, and SUN2) and co-staining with a general membrane marker Concanavalin A (ConA) (**Figures 2A-B and D**). In agreement with our TEM data, we observed that NE budding events occur almost exclusively in differentiated myotubes and are rarely found in undifferentiated myoblasts (**Figure 2C**). NE buds are not detected using antibodies against the ONM-residing protein Nesprin-3 nor are they wrapped by Lamin A/C, and they do not contain DNA (imaged with DAPI) (**Figure 2A-B and E**). These results are consistent with the inward topology of NE buds (Figure 1), and with previous literature suggesting that disassembly of the local lamina is required to facilitate INM budding for viral egress [30–34]. To assess the stability and dynamics of NE buds, we performed live-imaging fluorescence microscopy with the INM protein Lap1b mCherry-tagged. Live-imaging experiments revealed that NE buds persist over the course of 60 min time-lapse recordings, with minimal dynamics observed for 15 out of the 16 NE buds tracked (see representative example in **Figure 2F and Movie S1).** These data suggest that NE buds may represent a specialized domain of the INM, through which cargoes are transported within smaller, intraluminal vesicles (ILVs). This hypothesis is supported by our TEM observations, which show that most of NE buds contain ILVs. It is notable that these morphological features observed by fluorescence microcopy and TEM resemble the membrane remodeling pathway used by viruses during nuclear egress.

NE buds contain long sarcomeric transcripts

We performed fluorescence *in situ* hybridization (FISH) combined with immunofluorescence to investigate whether NE buds found in differentiated C2C12 myotubes contain endogenous transcripts. First, we used an oligo-dT (T30) probe to visualize general polyadenylated (poly-A) mRNAs in combination with antibodies against Emerin or Nesprin3 to visualize NE buds relative to the INM and ONM membranes (**Figure 3A-B**). These data confirmed that poly-A mRNAs are present in INM-derived NE buds. Next, we performed single molecule FISH (smFISH) to image a subset of endogenous mRNAs, including muscle-specific transcripts of different lengths and ubiquitously expressed control transcripts (**Figure 3C**). NE buds were labeled using the general membrane stain ConA as shown before (Figure 2). Due to the extremely long nature of the sarcomeric transcripts, two different sets of probes were used for Titin (100 kb) and Nebulin (26 kb) targeting the 3'- and the 5'-ends of the transcript to allow tracking of full-length mature transcripts (**Figure S1**). We found that about 70% of NE buds are enriched in Titin mRNA, and about 50% are enriched for Nebulin mRNA (**Figure 3C-D**). For both transcripts, probe sets targeting the 3'-end and the 5'-end of the mRNAs always co-localized within NE buds, suggesting that only full-length transcripts are incorporated into these structures (**Figure S1**). Notably, we did not detect a significant enrichment of other muscle-specific transcripts within NE buds, such as Myosin heavy chain 4 (Myh4, 6 kb) or Myosin light chain 4 (Myl4, 1 kb) mRNAs (**Figure 3C-D**). NE buds were also not enriched for AHNAK mRNA (18 kb), a long non-muscle specific transcript (**Figure 3C-D**). Moreover, NE buds did not contain the highly expressed housekeeping gene

transcript GAPDH (1.5 kb) nor the nuclear-localized long noncoding RNA (lncRNA), MALAT1 (7 kb) (**Figure 3C-D**). Since Titin and Nebulin are both sarcomeric component mRNAs found to be highly enriched within NE buds, we investigated whether these two mRNAs are components of the same RNP. We performed smFISH experiments to simultaneously image both Titin and Nebulin mRNAs (**Figure 3E-G**). We found that the majority of NE buds observed (57.8%) contain both Titin and Nebulin transcripts within their lumen (**Figure 3G**). Together, our RNA-imaging experiments suggest that NE buds contain a subset of mature, exceptionally long, muscle-specific transcripts, including Titin and Nebulin mRNAs.

Proximity proteomics identified the RBP UIF within NE buds

We designed protein proximity labeling experiments to identify the machinery involved in targeting cargo to NE buds. Our strategy was to fuse the INM protein Lap1b to the promiscuous biotin ligase TurboID [35]. We generated stable C2C12 cell lines expressing murine Lap1b-TurboID-mNeonGreen (see cartoon in **Figure 4A**). Myoblasts expressing the fusion protein were differentiated for 6 days into myotubes. After differentiation, biotin (500 μM) was added for 1 hour and we confirmed that NE buds could be biotinylated by fluorescence microscopy, using Alexa-conjugated streptavidin (**Figure 4B-C**). In parallel, we collected cell lysates post-biotin treatment, purified biotinylated proteins using a streptavidin affinity column, and identified purified proteins by mass spectrometry (**Figure S2**). As a control, we used proteins biotinylated from undifferentiated C2C12 myoblasts expressing Lap1b-TurboID-mNeonGreen, since their nuclei do not contain NE buds (Figures 1 and 2). Experiments were performed in triplicate, and only candidates enriched (based on both LFQ intensities and iBAQ values) relative to controls in at least 2 replicates were considered *bona fide* hits. Known Lap1b interactors, such as Torsin1A and Torsin1B, were equally represented in both myoblasts and myotubes samples (**Figure S2B**). Interestingly, several proteins were selectively enriched in differentiated myotubes, including approximately 40 proteins localized to the nucleus, NE or endoplasmic reticulum (**Figure 4D**). Among these, we focused on the RNA binding protein (RBP) UIF (UAP56-Interacting Factor, encoded by the Fyttd1 gene).

Two features make UIF a compelling candidate: (1) it has been reported to act as an alternative mRNA export adaptor in the transcription-export (TREX) pathway, recruited to mRNA by the RNA helicase DDX39B/UAP-56 [36]; and (2) it interacts with a Herpes Simplex 1 protein involved in exporting viral transcripts [37]. While we also detected DDX39B/UAP56 in our proteomics dataset, unlike UIF, this adaptor protein was equally biotinylated in undifferentiated myoblasts and differentiated myotubes (**Figure S2B**). We confirmed UIF expression by immunoblotting in both undifferentiated and differentiated C2C12 cells (**Figure S2C**). This observation aligns with findings of high UIF expression levels in skeletal muscle from several human gene expression databases (source: Human Protein Atlas). Next, we performed immunofluorescence experiments on differentiated C2C12 myotubes to assess whether UIF is found within NE buds. These experiments revealed that more than half of ConA-labeled NE buds contain UIF in their lumen (54%) (**Figure 4E-F**). In contrast, the canonical export factor DDX39B/UAP56, previously reported to interact with UIF [36], was only detected in 13% of visible NE buds (**Figure 4E-F**). Together, these results suggest a novel muscle-specific role for UIF in the context of NEB-associated export during myogenesis.

We then tested whether UIF is present in the lumen of NE buds that also contain mRNA cargoes. Endogenous UIF was imaged by immuno-staining in parallel with smFISH labeling of the large sarcomeric mRNAs, Titin or Nebulin, in ConA-Alexa488 labeled NE buds (**Figure 4G**). We observed a strong correlation whereby most NE buds that contain the UIF protein also contain Titin mRNAs (85%) while only a small portion of NE buds contain only UIF protein (12% of NE

buds) or Titin mRNA (3% of NE buds) (**Figure 4H**). These results demonstrate that the UIF protein is a reliable marker for NE buds containing endogenous mRNA cargoes, and it may play a role in trafficking cargoes to these NE buds.

The RBP UIF is required for mRNA recruitment to NE buds

To test whether UIF plays a role in trafficking large mRNA cargoes into NE buds, UIF was depleted from C2C12 cells using siRNAs transfected on day 3 of differentiation and analyzed three days later (at day 6) (see workflow in **Figure 5A**). UIF depletion was validated by reverse transcription of RNA followed by quantitative PCR (RT-qPCR) (**Figure S3A-C**), immunoblot analyses (**Figure 5B**), and immunofluorescence (**Figure 5C**). Myogenesis did not appear to be impaired by acute UIF depletion (between days 3-6), based on Myh4 protein levels and the persistence of multinucleated myotubes (**Figure 5B-C and Figure S3C**). UIF depletion also did not lead to a statistically significant change in the frequency of NE buds identified by ConA staining (**Figure 5D**). However, NE buds in nuclei of UIF-depleted myotubes contained significantly less Titin mRNA (visualized by smFISH), compared to the siRNA control (45% vs. 76%, **Figure 5E-F**). Next, we tested whether exclusion of Titin mRNA from NE buds would disrupt Titin mRNA export from the nucleus. We performed RT-qPCR on mRNA isolated from myonuclei purified from UIF-depleted and control myotubes (**Figure 5G and Figure S3A-C**). These experiments revealed that UIF depletion also led to a significant ~2-fold increase of Titin and Nebulin mRNA in myonuclei normalized to the control siRNA-treated myonuclei. Notably, we did not observe a similar accumulation in myonuclei for other transcripts, including Myh4 (which is not enriched within NE buds by smFISH, as shown in Figure 3C) and beta-Actin, suggesting that the canonical mRNA export pathway is not affected by UIF depletion. The total levels of Titin and Nebulin mRNA were also increased relative to other transcripts, likely due to an increased stability of the transcripts in the nucleus combined with their particularly long half-life (of about 3 days) [38] (**Figure S3C**). Together these results indicate that UIF functions to traffic large sarcomeric transcripts into NE buds and this pathway is relevant for their nuclear export.

ESCRT-III and CLCC1 are involved in NE budding

We have found that NE buds containing UIF and sarcomeric mRNAs in myotubes share some phenotypic and mechanistic similarities with NE buds that traffic viral nucleocapsids (see Figure 1 and 2). Two membrane remodeling machineries, ESCRTIII and CLCC1, have been reported in the literature to play defined and sequential roles in Herpesvirus nuclear egress [27,28], and thus may be also involved in the nuclear export of sarcomeric transcripts via NEB during myogenesis. In this context, it has been reported that ESCRT-III is the membrane remodeling machinery responsible for the scission of cargo-containing ILVs from the INM into the PNS [27]. To test a role for ESCRT-III in NEB of endogenous transcripts, we depleted two different components of the ESCRT-III machinery, Alix and CHMP4C, by RNA interference (RNAi) following the same depletion strategy used for UIF (see workflow in Figure 5A). The levels of Alix and CHMP4C depletion were measured by RT-qPCR relative to an siRNA control (**Figure 6A**, left and middle panels). Silencing of Alix or CHMP4C by this strategy did not impair the ability of C2C12 cells to further differentiate into myotubes (as demonstrated by unchanged myogenesis marker levels in **Figure 6A and Figure S4A**), nor did they statistically reduce the number of NE buds identified with ConA (**Figure 6B**). However, depletion of either Alix or CHMP4C led to a re-localization of UIF to the surface of NE buds, compared to control cells where UIF is normally internalized within the NE bud lumen (~ 50-60% vs. 21% in control, **Figure 6C-D**). This phenotype is consistent with a defect in the scission of INM-derived vesicles and a stalling of cargo on the surface of the main NE bud.

CLCC1 is a chloride channel that was recently shown to be required for the de-envelopment of Herpesvirus [28]. In this study, Dai and colleagues showed that CLCC1 depletion prevents vesicle fusion with the ONM, resulting in the accumulation of Herpesvirus-containing vesicles in the PNS. We therefore tested whether CLCC1 is also involved in UIF-dependent endogenous cargo export via NEB. CLCC1 was silenced in differentiating C2C12 myotubes using siRNAs at day 3, and phenotypes were analyzed at day 6 (as described before in Figure 5A workflow). RT-qPCR analyses confirmed ~50% reduction of CLCC1 transcripts relative to controls (**Figure 6A,** right panel). CLCC1 acute reduction did not appear to disrupt C2C12 differentiation between days 3 and 6 (**Figure S4B**). CLCC1 reduction also did not significantly affect the number of ConA-labeled NE buds (**Figure 6B**, right panel). However, the reduction in CLCC1 levels did cause a marked increase in NE bud diameter, with some structures reaching dimensions > 2 µm when measured by fluorescence microscopy (**Figure 6E-G**). We reasoned that an increase in NE bud volume could reflect the accumulation of ILVs that are stalled in the absence of CLCC1 within the main NE bud. This finding parallels the accumulation of Herpesvirus-containing vesicles in the PNS observed upon CLCC1 depletion in infected cells[28].

Next, we tested whether the phenotypes associated with the depletion of these two membrane remodeling machineries would impair nuclear export of NEB cargoes. We first scored whether the cellular distribution of endogenous UIF changes following Alix/ESCRTIII or CLCC1 depletion **(Figure 6H-I and S4C and E**). UIF distribution was analyzed by immunostaining and the mean fluorescence intensity in nuclei depleted for ESCRT-III or CLCC1 was quantified, compared to controls. Depletion of either Alix or CLCC1 led to a significant accumulation of UIF in the nucleus, possibly reflecting a disruption in its trafficking (**Figure 6H-I**). Next, we performed RT-qPCR analysis of mRNA isolated from fractionated myonuclei of myotubes following Alix or CLCC1 depletion (**Figure 6J-K**). These experiments revealed that either Alix or CLCC1 depletion led to a statistically significant ~2-fold increase of Titin and Nebulin mRNAs in myotube nuclei compared to control siRNA-treated myotubes, indicating accumulation of these mRNAs in myonuclei similar to what we previously detected with UIF depletion (Figure 5F-G). Control mRNAs that are not found enriched in NE buds by smFISH were not affected, indicating that NPC-mediated export remains functional. The total levels of Titin and Nebulin mRNA were also increased relative to other transcripts (**Figure S4D and S4F**), similar to results in UIF-depleted myotubes (Figure S3C). Together, these results reveal that depletion of either ESCRT-III or CLCC1 machineries, results in a selective NEB-dependent nuclear export defect. We conclude that two of the same membrane remodeling machineries that Herpesviruses co-opts for nuclear egress may work sequentially to facilitate trafficking of endogenous cargo through NE buds.

DISCUSSION

Our research demonstrates for the first time that NEB plays an important role in mRNA export in mammalian cells, with a particular focus on skeletal muscle and myogenesis. We provide multiple lines of evidence supporting the existence of NEB as an alternative nuclear export process involved in the transport of large sarcomeric transcripts during myogenesis. Our data demonstrate that most NE buds observed in myotubes contain Titin and Nebulin transcripts, often co-localizing within the same NE bud (**Figure 3**). In contrast, we did not observe a clear enrichment of the other selected transcripts we analyzed, including shorter muscle-specific transcripts (Myh4 and Myl4), as well as other ubiquitously expressed long transcripts (AHNAK) (**Figure 3C-D**). These results suggest the existence of a mechanism of NEB cargo selectivity.

How transcripts are selected to be exported via NEB remains an open question. Potential selectivity mechanisms could either be based on mRNA sequence, likely mediated by specific

RNA binding proteins (RBPs), or be size-dependent. To identify RBPs involved in NEB, we used a localized proximity proteomics approach, which led to the identification of UIF (**Figure 4 and Figure S2**). Our data demonstrated that UIF is a reliable marker for identifying NE buds that contain mRNA cargoes (**Figure 4G-H**). Importantly, UIF depletion reduces mRNA internalization into NE buds and correspondingly increases mRNA cargoes levels in the nucleus (Titin and Nebulin, shown in **Figure 5E-G**). Together, these results suggest that UIF plays a role in targeting large endogenous mRNAs to NE buds for NEB-mediated export. UIF has previously been reported to interact with a Herpesvirus protein involved in viral nuclear egress [38] which further supports the idea that viruses may have co-opted this host RNA export factor. In agreement with this, it has been reported that UIF transcript levels are particularly high in lymphocytes transduced with Epstein-Barr Virus (EBV), a member of the Herpesvirus family (source: GTEx portal, GTEx Analysis Release V10).

The membrane remodeling events that lead to NEB are fascinating (**Figure 7** model). Our electron and fluorescence imaging data demonstrate that NE buds originate from the INM, protrude inward into the nucleoplasm and are not lined with a lamin coat (**Figures 1-2**). The inward topology, the presence of ILVs (**Figure 1G-K**) and the size of NE buds (**Figure 1F**) are consistent with previous reports of NEB in the post-synaptic side of the NMJ in Drosophila [26,39–42]. Those morphological features of NE buds and their inclusions also closely resemble membrane remodeling events that are reported during nuclear egress of Herpesviruses [6]. Based on the morphological similarities observed between NEB and viral nuclear egress, we investigated the role of ESCRT-III and CLCC1 (**Figure 6**). Our data confirm that these factors are involved in NEB of endogenous RNPs. Depletion of CLCC1 or ESCRT-III share common phenotypes in that they lead to accumulation of UIF and cargo in the nucleus. However, CLCC1 and ESCRT-III depletion affects NE bud morphology in different ways that draws compelling parallels to their roles during viral egress [27,28]. NE buds in ESCRT-III depleted cells accumulate UIF around their surfaces, which is the phenotype one would expect if ILVs are stalled around the NE bud because their scission is affected. Whereas CLCC1 depletion leads to NE buds that still have UIF within their lumen but are now highly enlarged likely because ILVs can no longer fuse with the ONM to release their cargo, and they accumulate in the PNS. Our future studies will clarify and expand on the role of ESCRT-III and CLCC1 during NEB and will aim to identify other factors involved in the different membrane remodeling steps required for NEB to occur.

Estimating the predicted size of RNPs containing extremely large transcripts is important to evaluate because it can reveal whether NEB is a necessary alternative to the ~60 nm-wide NPC channel [5]. We expect that mRNAs this large might need to be compacted to fit into the ILVs that we have measured (**Figure 1I**). A plausible model to estimate Titin compaction into an RNP is based on comparison with Balbiani bodies. In the case of Balbiani bodies it was experimentally demonstrated that a 37,000 nucleotides long transcript can compact together with proteins into an RNPs with a diameter of ~50 nm [43–45]. Considering Titin mRNA length of 100,000 nucleotides, and assuming spherical shape, similar compaction, and similar mRNA-protein ratio, one could predict that an RNP containing a single molecule of Titin would be about 3 times larger, reaching a diameter of about 70 nm. From our electron microscopy measurements, displaying an average ILV diameter of ~170 nm (**Figure 1I**), ILVs could easily accommodate multiple RNPs of this size. It is also relevant to consider that these extremely long transcripts are also highly expressed during myogenesis. Thus, trying to export them through the NPC could potentially stall and block NPC-mediated transport, possibly signaling to redirect these oversized cargoes for transport via NEB. In this scenario, NEB may represent a more efficient route for the export of RNPs composed of large sarcomeric mRNAs.

The presence of uniquely large and abundant transcripts in NE buds, combined with the post-mitotic nature of myotubes (hence, the lack of major NE rearrangements that could allow passive export of large cargoes), both represent favorable conditions for NEB to occur. It is also reasonable to think that NEB might not be exclusively present in skeletal muscle cells. Our future studies will explore NEB-mediated RNP export in other specialized post-mitotic mammalian cell types, such as neurons and dendritic cells.

Limitations of this study

The observation that only a subset of the mRNAs analyzed was found within NE buds suggests the existence of a selective mechanism responsible for the recruitment of mRNA to NEB events. However, it is important to highlight that the absence of an smFISH signal from NE buds in our experiments does not rule out transcript presence within these structures, as the sensitivity of this method strongly relies on the abundance of the transcript analyzed. Considering this technical limitation, and the fact that this study was limited to a selected list of transcripts, further work using alternative high-throughput approaches will be required to clarify and expand the transcriptome of NE buds in muscle cells. Another relevant aspect to note is that acute depletion of UIF, ESCRT-III, and CLCC1 during myogenesis did not impact on the ability of myotubes to differentiate. Impairing Titin (and other sarcomeric mRNAs) export from the nucleus would be expected to cause a defect in muscle differentiation. However, given the exceptionally long half-life of Titin mRNA and protein (72 hours for both) [38], it is likely that the 72-hour siRNA-mediated knockdown treatment used in our experiments was not sufficient to affect myogenesis.

ACKNOWLEDGMENTS

We thank R. Parker, B. Olwin, and J. Olzmann for helpful discussions and sharing materials. We thank the Boulder EM Service facility, especially G. Morgan and E. O'Toole, for technical advice and assistance. We thank E. Sawyer, M. Hoyer and the current and past members of the Voeltz lab for helpful discussions over the years and feedback on this manuscript. G.K.V. is an Investigator of the Howard Huges Medical Institute. S.Z. was supported by an Early.Postdoc.Mobility fellowship from the Swiss National Science Foundation and a long-term postdoctoral fellowship from Human Frontier Science Program (LT-000527/2021-L).

AUTHOR CONTRIBUTIONS

S.Z. and G.K.V. designed the research plan and interpreted the results. S.Z., J.B.M., and R.G.A. performed experiments and analyzed the results. S.Z. wrote the manuscript. G.K.V. edited and revised the manuscript.

REFERENCES

1. Pawar, S., and Kutay, U. (2021). The Diverse Cellular Functions of Inner Nuclear Membrane Proteins. Cold Spring Harb Perspect Biol *13*. https://doi.org/10.1101/CSHPERSPECT.A040477.

2. Ungricht, R., and Kutay, U. (2015). Establishment of NE asymmetry—targeting of membrane proteins to the inner nuclear membrane. Curr Opin Cell Biol *34*, 135–141. https://doi.org/10.1016/J.CEB.2015.04.005.

3. Grunwald, D., Singer, R.H., and Rout, M. (2011). Nuclear export dynamics of RNA-protein complexes. Nature *475*, 333–341. https://doi.org/10.1038/nature10318.

4. Petrovic, S., Mobbs, G.W., Bley, C.J., Nie, S., Patke, A., and Hoelz, A. (2022). Structure and Function of the Nuclear Pore Complex. Cold Spring Harb Perspect Biol *14*. https://doi.org/10.1101/cshperspect.a041264.

5. Zimmerli, C.E., Allegretti, M., Rantos, V., Goetz, S.K., Obarska-Kosinska, A., Zagoriy, I., Halavatyi, A., Hummer, G., Mahamid, J., Kosinski, J., et al. (2021). Nuclear pores dilate and constrict in cellulo. Science (1979) *374*, eabd9776. https://doi.org/10.1126/science.abd9776.

6. Klupp, B.G., and Mettenleiter, T.C. (2023). The Knowns and Unknowns of Herpesvirus Nuclear Egress. Annu Rev Virol *10*, 305–323. https://doi.org/10.1146/annurev-virology-111821-105518.

7. Johnson, D.C., and Baines, J.D. (2011). Herpesviruses remodel host membranes for virus egress. Nat Rev Microbiol *9*, 382–394.

8. Bigalke, J.M., and Heldwein, E.E. (2015). The Great (Nuclear) Escape: New Insights into the Role of the Nuclear Egress Complex of Herpesviruses. J Virol *89*, 9150–9153. https://doi.org/10.1128/JVI.02530-14.

9. Gay, H. (1955). Nucleo-cytoplasmic relations in salivary-gland cells of Drosophila. Proc Natl Acad Sci U S A *41*, 370–375. https://doi.org/10.1073/pnas.41.6.370.

10. Hadek, R., and Swift, H. (1962). Nuclear extrusion and intracisternal inclusions in the rabbit blastocyst. J Cell Biol *13*, 445.

11. Szollosi, M.S., and Szollosi, D. (1988). “Blebbing” of the nuclear envelope of mouse zygotes, early embryos and hybrid cells. J Cell Sci *91 (Pt 2)*, 257–267. https://doi.org/10.1242/jcs.91.2.257.

12. Szollosi, D. (1965). Extrusion of nucleoli from pronuclei of the rat. J Cell Biol *25*, 545–562. https://doi.org/10.1083/jcb.25.3.545.

13. Hochstrasser, M., and Sedat, J.W. (1987). Three-dimensional organization of Drosophila melanogaster interphase nuclei. II. Chromosome spatial organization and gene regulation. J Cell Biol *104*, 1471–1483. https://doi.org/10.1083/jcb.104.6.1471.

14. LaMassa, N., Arenas-Mena, C., and Phillips, G.R. (2018). Electron microscopic characterization of nuclear egress in the sea urchin gastrula. J Morphol *279*, 609–615. https://doi.org/10.1002/jmor.20796.

15. Keuenhof, K.S., Kohler, V., Broeskamp, F., Panagaki, D., Speese, S.D., Buttner, S., and Hoog, J.L. (2023). Nuclear envelope budding and its cellular functions. Nucleus *14*, 2178184. https://doi.org/10.1080/19491034.2023.2178184.

16. Rose, A., and Schlieker, C. (2012). Alternative nuclear transport for cellular protein quality control. Trends Cell Biol *22*, 509–514. https://doi.org/10.1016/j.tcb.2012.07.003.

17. Webster, B.M., Colombi, P., Jäger, J., and Lusk, C.P. (2014). Surveillance of nuclear pore complex assembly by ESCRT-III/Vps4. Cell *159*, 388–401.

18. Webster, B.M., Thaller, D.J., Jäger, J., Ochmann, S.E., Borah, S., and Lusk, C.P. (2016). Chm7 and Heh1 collaborate to link nuclear pore complex quality control with nuclear envelope sealing. EMBO J *35*, 2447–2467.

19. Wente, S.R., and Blobel, G. (1993). A temperature-sensitive NUP116 null mutant forms a nuclear envelope seal over the yeast nuclear pore complex thereby blocking nucleocytoplasmic traffic. J Cell Biol *123*, 275–284.

20. Dou, Z., Xu, C., Donahue, G., Shimi, T., Pan, J.-A., Zhu, J., Ivanov, A., Capell, B.C., Drake, A.M., and Shah, P.P. (2015). Autophagy mediates degradation of nuclear lamina. Nature *527*, 105–109.

21. Onischenko, E., Tang, J.H., Andersen, K.R., Knockenhauer, K.E., Vallotton, P., Derrer, C.P., Kralt, A., Mugler, C.F., Chan, L.Y., and Schwartz, T.U. (2017). Natively unfolded FG repeats stabilize the structure of the nuclear pore complex. Cell *171*, 904-917. e19.

22. Koch, B., and Yu, H.-G. (2019). Regulation of inner nuclear membrane associated protein degradation. Nucleus *10*, 169–180.

23. Lee, C.-W., Wilfling, F., Ronchi, P., Allegretti, M., Mosalaganti, S., Jentsch, S., Beck, M., and Pfander, B. (2020). Selective autophagy degrades nuclear pore complexes. Nat Cell Biol *22*, 159–166.

24. Chandra, S., Mannino, P.J., Thaller, D.J., Ader, N.R., King, M.C., Melia, T.J., and Lusk, C.P. (2021). Atg39 selectively captures inner nuclear membrane into lumenal vesicles for delivery to the autophagosome. Journal of Cell Biology *220*, e202103030.

25. Mannino, P.J., and Lusk, C.P. (2022). Quality control mechanisms that protect nuclear envelope identity and function. Journal of Cell Biology *221*, e202205123.

26. Speese, S.D., Ashley, J., Jokhi, V., Nunnari, J., Barria, R., Li, Y., Ataman, B., Koon, A., Chang, Y.T., Li, Q., et al. (2012). Nuclear envelope budding enables large ribonucleoprotein particle export during synaptic Wnt signaling. Cell *149*, 832–846. https://doi.org/10.1016/j.cell.2012.03.032.

27. Arii, J., Watanabe, M., Maeda, F., Tokai-Nishizumi, N., Chihara, T., Miura, M., Maruzuru, Y., Koyanagi, N., Kato, A., and Kawaguchi, Y. (2018). ESCRT-III mediates budding across the inner nuclear membrane and regulates its integrity. Nat Commun *9*, 3379.

28. Dai, B., Polack, L., Sperl, A., Dame, H., Huynh, T., Deveney, C., Lee, C., Doench, J.G., and Heldwein, E.E. (2024). CLCC1 promotes membrane fusion during herpesvirus nuclear egress. bioRxiv. https://doi.org/10.1101/2024.09.23.614151.

29. Panagaki, D., Croft, J.T., Keuenhof, K., Larsson Berglund, L., Andersson, S., Kohler, V., Buttner, S., Tamas, M.J., Nystrom, T., Neutze, R., et al. (2021). Nuclear envelope budding is a response to cellular stress. Proc Natl Acad Sci U S A *118*. https://doi.org/10.1073/pnas.2020997118.

30. Muranyi, W., Haas, J., Wagner, M., Krohne, G., and Koszinowski, U.H. (2002). Cytomegalovirus recruitment of cellular kinases to dissolve the nuclear lamina. Science

(1979) *297*, 854–857. https://doi.org/10.1126/SCIENCE.1071506/SUPPL_FILE/1071506S3_THUMB.GIF.

31. Scott, E.S., and O'Hare, P. (2001). Fate of the Inner Nuclear Membrane Protein Lamin B Receptor and Nuclear Lamins in Herpes Simplex Virus Type 1 Infection. J Virol *75*, 8818–8830. https://doi.org/10.1128/JVI.75.18.8818-8830.2001/ASSET/B55632A8-B431-40B5-948B-BACAAA6BCDBD/ASSETS/GRAPHIC/JV1810635008.JPEG.

32. Reynolds, A.E., Liang, L., and Baines, J.D. (2004). Conformational Changes in the Nuclear Lamina Induced by Herpes Simplex Virus Type 1 Require Genes U L 31 and U L 34 . J Virol *78*, 5564–5575. https://doi.org/10.1128/JVI.78.11.5564-5575.2004/ASSET/F8F41D26-B5F4-480D-B7B0-F09A74D77EE9/ASSETS/GRAPHIC/ZJV0110446660007.JPEG.

33. Simpson-Holley, M., Baines, J., Roller, R., and Knipe, D.M. (2004). Herpes Simplex Virus 1 U L 31 and U L 34 Gene Products Promote the Late Maturation of Viral Replication Compartments to the Nuclear Periphery . J Virol *78*, 5591–5600. https://doi.org/10.1128/JVI.78.11.5591-5600.2004/ASSET/6F19A87A-09CD-488D-8FED-ED6E1F9F745D/ASSETS/GRAPHIC/ZJV0110446670006.JPEG.

34. Simpson-Holley, M., Colgrove, R.C., Nalepa, G., Harper, J.W., and Knipe, D.M. (2005). Identification and Functional Evaluation of Cellular and Viral Factors Involved in the Alteration of Nuclear Architecture during Herpes Simplex Virus 1 Infection. J Virol *79*, 12840–12851. https://doi.org/10.1128/JVI.79.20.12840-12851.2005/ASSET/4FE6ED20-2899-4115-8756-D4D05573508E/ASSETS/GRAPHIC/ZJV0200569150005.JPEG.

35. Branon, T.C., Bosch, J.A., Sanchez, A.D., Udeshi, N.D., Svinkina, T., Carr, S.A., Feldman, J.L., Perrimon, N., and Ting, A.Y. (2018). Efficient proximity labeling in living cells and organisms with TurboID. Nat Biotechnol *36*, 880–887.

36. Hautbergue, G.M., Hung, M.-L., Walsh, M.J., Snijders, A.P.L., Chang, C.-T., Jones, R., Ponting, C.P., Dickman, M.J., and Wilson, S.A. (2009). UIF, a New mRNA export adaptor that works together with REF/ALY, requires FACT for recruitment to mRNA. Current Biology *19*, 1918–1924.

37. Tunnicliffe, R.B., Tian, X., Storer, J., Sandri-Goldin, R.M., and Golovanov, A.P. (2018). Overlapping motifs on the herpes viral proteins ICP27 and ORF57 mediate interactions with the mRNA export adaptors ALYREF and UIF. Sci Rep *8*, 15005.

38. Cadar, A.G., Zhong, L., Lin, A., Valenzuela, M.O., and Lim, C.C. (2014). Upstream Open Reading Frame in 5′-Untranslated Region Reduces Titin mRNA Translational Efficiency. Biochem Biophys Res Commun *453*, 185. https://doi.org/10.1016/J.BBRC.2014.09.085.

39. Davidson, K.A., Nakamura, M., Verboon, J.M., and Parkhurst, S.M. (2023). Centralspindlin proteins Pavarotti and Tumbleweed along with WASH regulate nuclear envelope budding. Journal of Cell Biology *222*, e202211074.

40. Verboon, J.M., Nakamura, M., Davidson, K.A., Decker, J.R., Nandakumar, V., and Parkhurst, S.M. (2020). Drosophila Wash and the Wash regulatory complex function in nuclear envelope budding. J Cell Sci *133*, jcs243576.

41. Jokhi, V., Ashley, J., Nunnari, J., Noma, A., Ito, N., Wakabayashi-Ito, N., Moore, M.J., and Budnik, V. (2013). Torsin mediates primary envelopment of large ribonucleoprotein granules at the nuclear envelope. Cell Rep *3*, 988–995. https://doi.org/10.1016/j.celrep.2013.03.015.

42. Li, Y., Hassinger, L., Thomson, T., Ding, B., Ashley, J., Hassinger, W., and Budnik, V. (2016). Lamin Mutations Accelerate Aging via Defective Export of Mitochondrial mRNAs through Nuclear Envelope Budding. Curr Biol *26*, 2052–2059. https://doi.org/10.1016/j.cub.2016.06.007.

43. Björk, P., Jin, S.B., Zhao, J., Singh, O.P., Persson, J.O., Hellman, U., and Wieslander, L. (2009). Specific combinations of SR proteins associate with single pre-messenger RNAs in vivo and contribute different functions. Journal of Cell Biology *184*, 555–568. https://doi.org/10.1083/JCB.200806156.

44. Skoglund, U., Andersson, K., Björkroth, B., Lamb, M.M., and Daneholt, B. (1983). Visualization of the formation and transport of a specific hnRNP particle. Cell *34*, 847–855. https://doi.org/10.1016/0092-8674(83)90542-1.

45. Mehlin, H., Daneholt, B., and Skoglund, U. (1992). Translocation of a specific premessenger ribonucleoprotein particle through the nuclear pore studied with electron microscope tomography. Cell *69*, 605–613. https://doi.org/10.1016/0092-8674(92)90224-Z.

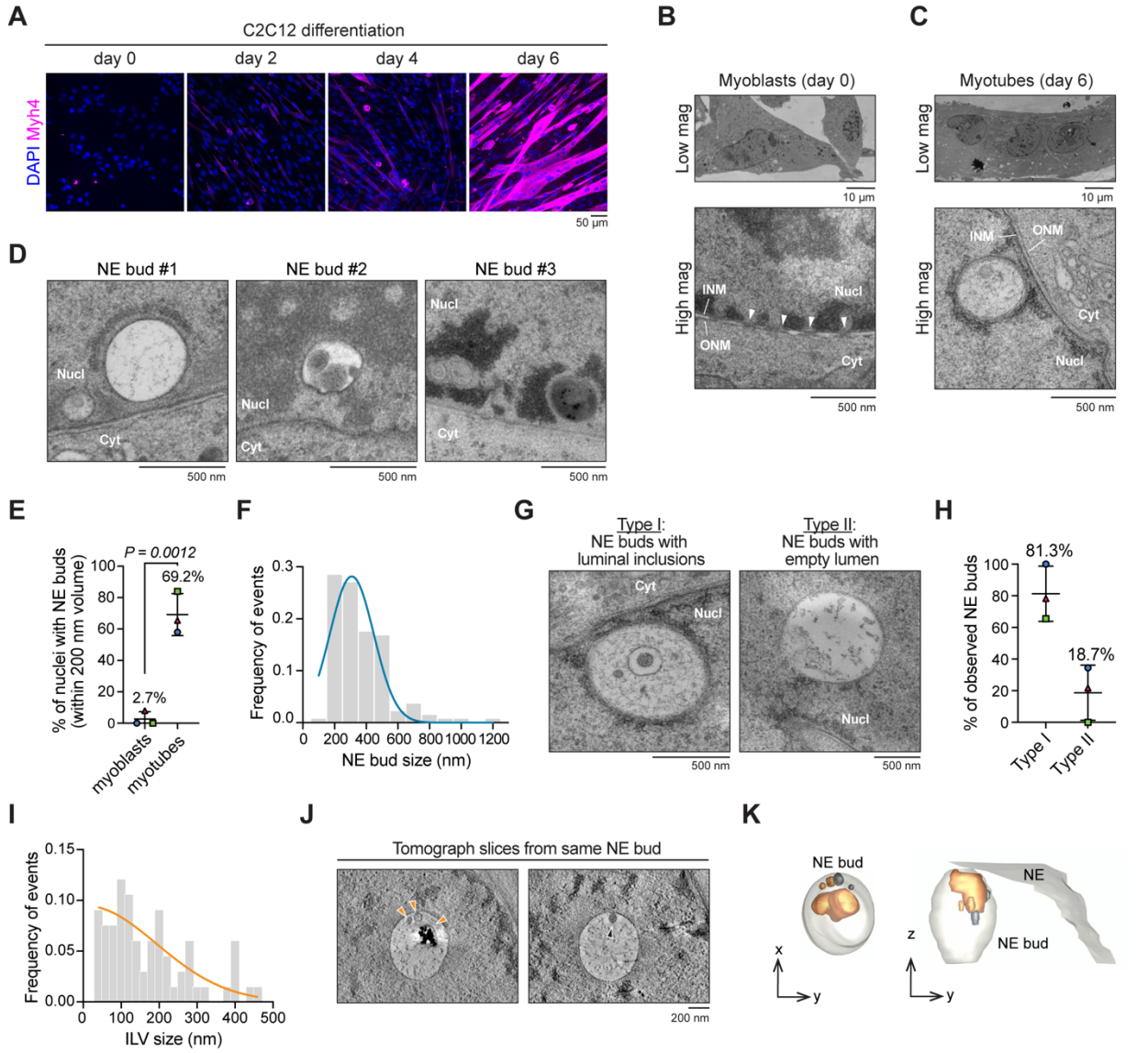

Figure 1. TEM identifies NE buds with internal luminal vesicles (ILVs) in nuclei of differentiated C2C12 myotubes

(**A**) C2C12 cells were immunostained with an antibody against Myosin heavy chain 4 (Myh4; magenta) and stained with DAPI (DNA; blue) at day 0, 2, 4 and 6 of differentiation. (**B-C**) Electron micrographs of NE in C2C12 cells pre- (myoblasts) (B) or 6 days post-differentiation into myotubes (C). Arrowheads in (B) indicate NPCs; nucleus (Nucl) and cytoplasm (Cyt) are labeled for clarity. (**D**) Additional examples of NE buds from day 6 myotubes. (**E**) Percent of nuclei with 1 or more NE buds present at day 0 (myoblast) or after 6 days of differentiation (myotubes) quantified from NE buds visualized in ≥2 consecutive TEM serial thin sections (for a total nuclear volume ≥200nm) (n= 54 and 67 nuclei analyzed from myoblasts and myotubes, respectively). Mean and standard deviation are represented in the graph. (**F**) Distribution of frequency of NE bud diameters measured from TEM serial sections (90 nm thickness each section). Frequency of events is represented as the fraction of NE buds in each binning range on the total of NE buds analyzed (equal to 1). A Gaussian fit is represented in blue (n=137 NE buds). (**G**) Representative images and (**H**) frequency of the two most common NE bud morphologies with luminal inclusions (Type I)

or without (Type II) found in C2C12 myotubes (n = 137 NE buds). (**I**) Distribution of frequency of ILV diameters measured from TEM serial sections (90 nm thickness each section). Frequency of events is represented as the fraction of ILVs in each binning range on the total of ILVs analyzed (equal to 1). A Gaussian fit is represented in orange (n=66 ILVs measured from 2 independent biological replicates). (**J**) EM tomograph and (**K**) corresponding 3D model of a NE bud revealing nascent and internalized luminal inclusions. Orange and black arrowheads in (J) indicate internal inclusions (orange) or vesicles in the process of budding (black), represented in the model in (K). All experiments were performed in n = 3 independent biological replicates, unless stated otherwise. Scale bars are reported below every image.

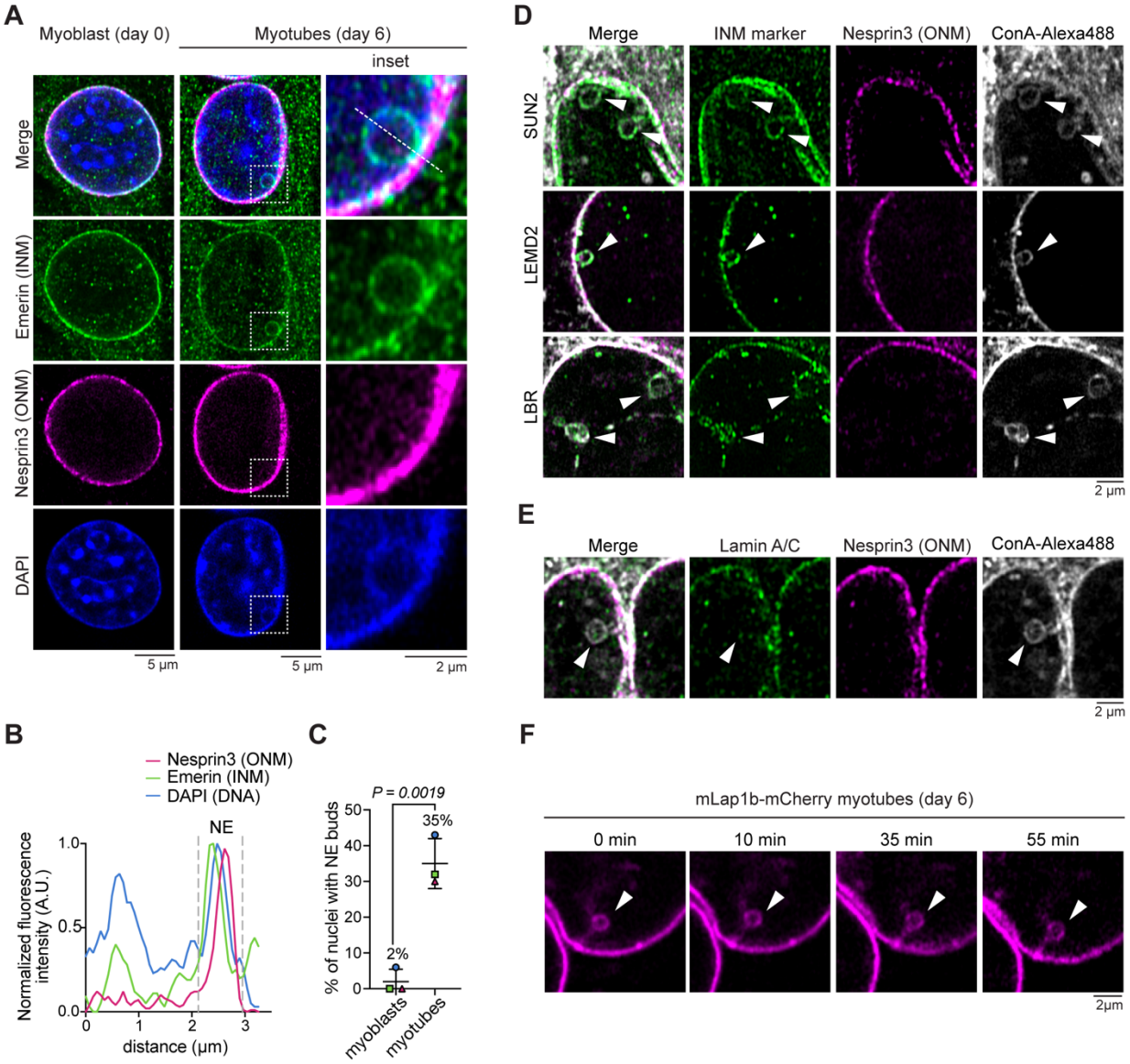

Figure 2. Large inward NE buds originate from the INM in nuclei of differentiated myotubes

(**A**) C2C12 cells were immunostained with antibodies against the endogenous ONM protein Nesprin3 (magenta) and INM protein Emerin (green) in C2C12 myoblasts (day 0) or myotubes (day 6 of differentiation). DAPI (blue) was used to label DNA. Dashed boxes indicate the magnified area shown on the right. (**B**) Relative fluorescence intensity profile for Emerin, Nesprin3 and DNA from line-scan shown in (A) indicates that only Emerin is present at the membrane of the bud. (**C**) Frequency of nuclei containing one or more observable Emerin-labeled NE buds in C2C12 myoblasts and myotubes (day 6 of differentiation). Mean and standard deviation are represented in the graph. (**D**) NE bud immunostaining with antibodies against the endogenous ONM protein Nesprin3 (magenta) in combination with several different INM components (green), including SUN2, LEMD2, or LBR. Concanavalin A (ConA-Alexa488) was used as a general membrane marker to label NE buds (grey; marked with white arrowheads). (**E**) Immunostaining with an antibody against endogenous Lamin A/C shows that it does not localize to NE buds in C2C12 myotubes. Neither LaminA/C (green) nor the ONM marker Nesprin3 (magenta) co-localize with the NE bud labeled with ConA-Alexa488 (marked with white arrowheads). (**F**) Representative time lapse

series of an NE bud (marked with a white arrowhead) in myotubes stably expressing murine Lap1b fused with mCherry (mLap1b-mCherry) (magenta) (n=16 NE buds from 3 independent biological replicates). Note that 15 out of the 16 NE buds analyzed persist over 60 min, without significant changes in their size or shape. Time points are reported above each frame. All experiments were performed in n = 3 independent biological replicates, unless stated otherwise. Scale bars are reported below every image.

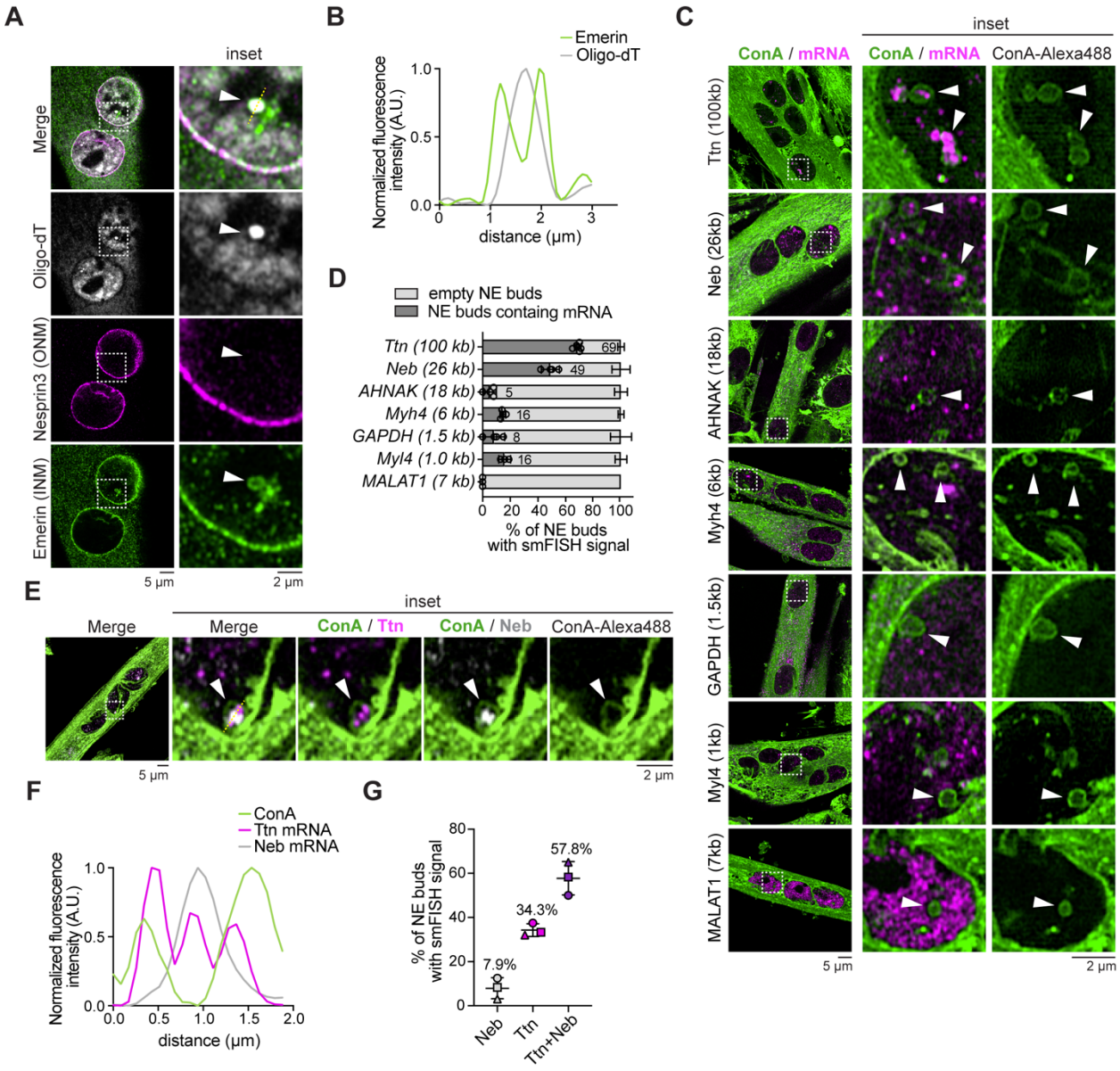

Figure 3. Titin and Nebulin transcripts are selectively enriched in NE buds

(**A**) C2C12 myotube nuclei were immunostained with antibodies against Emerin (INM; green) and Nesprin3 (ONM; magenta) to identify the NE buds (marked by white arrowhead) and to detect whether they contain poly-A transcripts by FISH (grey; oligo-dT$_{30}$ probe). Dashed boxes indicate the magnified area shown on the right. (**B**) Fluorescence intensity profile of NE bud highlighted in (A) confirms poly-A transcripts in an Emerin-labeled NE bud. (**C**) To identify whether select transcripts are found in NE buds, single molecule FISH (smFISH) was performed using probe sets targeting various muscle-specific and housekeeping transcripts (magenta). NE buds were identified using ConA-Alexa488 labeling (green; marked with white arrowheads). For Titin (Ttn) and Nebulin (Neb) 3'-end probe sets are shown to ensure that full-length transcripts are imaged. Note that smFISH against Ttn and Neb reveals punctate accumulation of these transcripts in NE buds. AHNAK was used as a non-muscle specific long transcript control, while the nuclear lncRNA MALAT1 was used as a negative control. Magnified images of regions in dashed boxes are shown in right panels. (**D**) Frequency of various muscle- and non-muscle specific transcript enrichment within NE buds quantified from experiment described in (C). Mean and standard deviation are represented in the

graph. (**E**) Ttn (3'-end probes; magenta) and Neb (5'-end probes; grey) smFISH shows co-localization of the two transcripts within the same ConA-Alexa488 labeled NE bud (green; marked with white arrowheads). Magnified images of regions in dashed boxes are shown in right panels. (**F**) Fluorescence intensity profile of line scan shown in (E) shows that both transcripts are enclosed within the NE bud. (**G**) Co-localization frequency of Ttn and Neb transcripts within the same NE bud (n= 59 NE buds analyzed). Mean and standard deviation are represented in the graph. All experiments were performed with n = 3 independent biological replicates, unless stated otherwise. Scale bars are reported below every image.

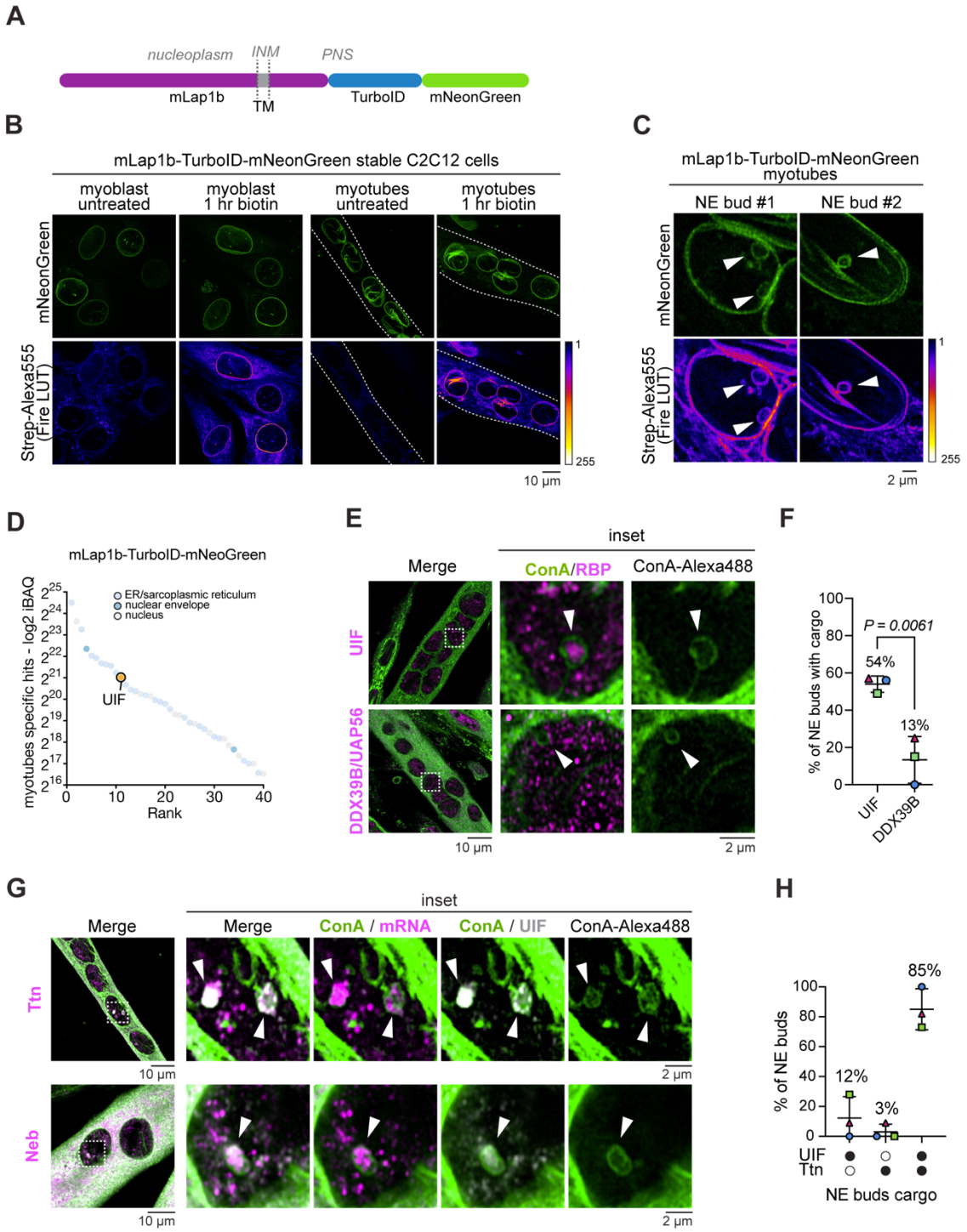

Figure 4. Identification of UIF as a NEB-associated protein by proximal proteomics

(**A**) Cartoon diagram and domain organization of murine Lap1b-TurboID-mNeonGreen fusion construct used for proximity proteomics. TM = transmembrane domain. (**B**) Representative images of C2C12 myoblasts and myotubes, untreated or treated with 500 µM biotin for 1 hour prior to fixation. Localization of biotinylation *in situ* was observed by labeling with Streptavidin-Alexa555. Streptavidin signal co-localizes well with Lap1b-TurboID-mNeonGreen (green) at the NE. Fire LUT is used to emphasize intensity

difference. White dashed lines outline myotubes. (**C**) Examples of NE bud biotinylation (Strepativin-Alexa555; Fire LUT) from myotubes expressing mLap1b-TurboID-mNeonGreen (green). Fire LUT is used to emphasize intensity difference. NE buds are indicated by white arrowheads. (**D**) Proximity proteomic hits biotinylated in differentiated C2C12-derived myotubes but not myoblasts, ranked based on the average iBAQ values from the three independent experiments. endoplasmic reticulum (ER), NE and nuclear proteins are highlighted as described in the legend. (**E**) C2C12 myotubes were immunostained with antibodies against endogenous UIF or DDX39B/UAP56 (magenta). NE buds are labeled with ConA-Alexa488 (green; marked with white arrowheads). Magnified images of regions in dashed boxes are shown in right panels. (**F**) Frequency of UIF vs. DDX39B/UAP56 enrichment in NE buds in C2C12 myotubes. UIF shows the highest enrichment in NE buds. **(G**) Representative images of differentiated C2C12 cells immunostained with an antibody against endogenous UIF (grey) and co-labeled with smFISH 3'-end probes against Titin (Ttn) or Nebulin (Neb) transcripts as indicated (magenta) along with ConA-Alexa488 to identify NE buds (green; marked by white arrowheads). Magnified images of regions in dashed boxes are shown in right panels. (**H**) Frequency of UIF and Ttn co-localization within the same NE bud. Mean and standard deviation are represented. All experiments were performed with n = 3 independent biological replicates. Scale bars are reported below every image.

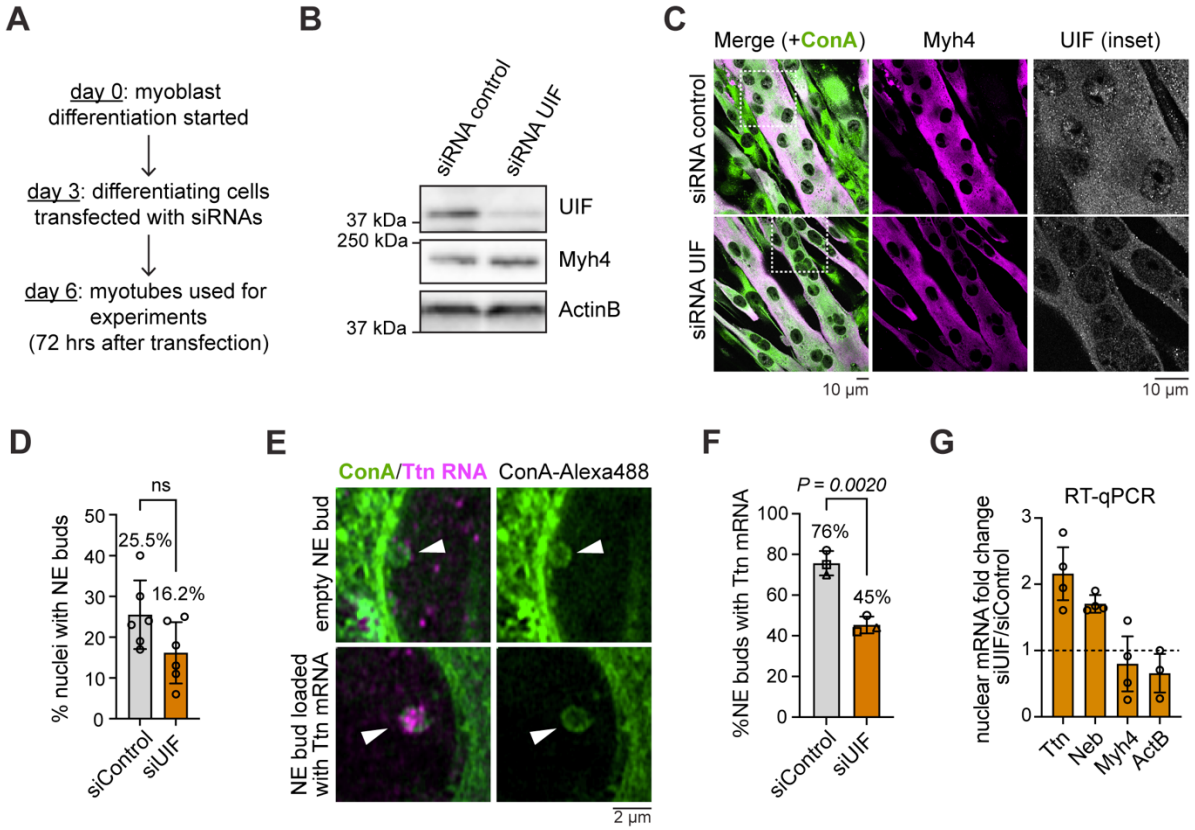

Figure 5. UIF regulates mRNA recruitment to NE buds

(**A**) Schematic representation of siRNA transfection protocol. (**B**) Immunoblot analysis confirmed that UIF is depleted by siRNA treatment relative to a control siRNA in differentiated myotubes. Myosin heavy chain 4 (Myh4) and beta-Actin were compared as loading and differentiation controls respectively. (**C**) Representative images of myotubes transfected with siRNA targeting UIF or control siRNA. Immunostaining with an antibody against endogenous UIF (grey) was used to identify knockdown cells. An antibody against Myh4 (magenta) was also used to verify myotube differentiation. ConA-Alexa488 (green) was used to identify NE buds. Magnified images of regions in dashed boxes are shown in right panels. (**D**) Frequency of NEB events in C2C12 myotubes following UIF depletion or control treatment. Mean and standard deviation are represented (n=6 independent biological replicates). (**E**) Representative images of NE buds labeled with ConA-Alexa488 (green; marked with white arrowheads) in siRNA depleted myotubes (as in C-F). 3'end-probes against Titin (Ttn) transcript (magenta) were used to test for the presence of the mRNA within NE buds. (**F**) Frequency of NE buds containing Ttn mRNA, scored from data shown in (E). Mean and standard deviation are represented. (**G**) RT-qPCR analysis of mRNA extracted from fractionated nuclei of myotubes transfected with siRNA targeting UIF or control siRNAs. Note that a nuclear increase is observed in Ttn and Nebulin (Neb) transcripts (reported as fold change of UIF-depleted relative to control samples) relative to no increase for Myh4 and beta-Actin (ActB) control transcripts, which are not localized to NE buds. Mean and standard deviation are represented. All experiments were performed with n = 3 independent biological replicates, unless stated otherwise. Scale bars are reported below every image.

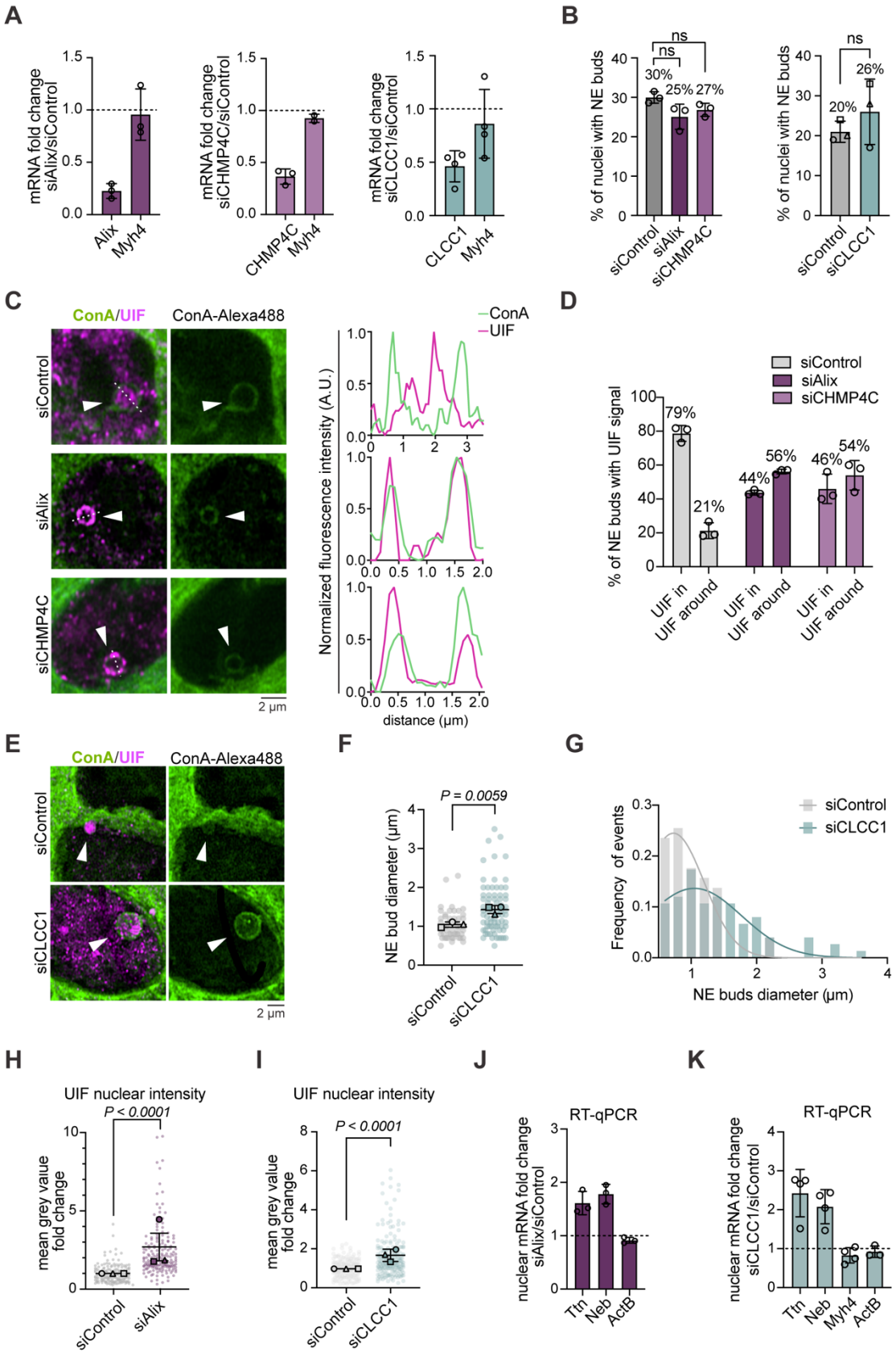
A
mRNA fold change siAlix/siControl
Alix
Myh4
mRNA fold change siCHMP4C/siControl
CHMP4C
Myh4
mRNA fold change siCLCC1/siControl
CLCC1
Myh4
B
% of nuclei with NE buds
ns
ns
30%
25%
27%
siControl
siAlix
siCHMP4C
20%
26%
siControl
siCLCC1
C
ConA/UIF
ConA-Alexa488
siControl
siAlix
siCHMP4C
2 µm
ConA
UIF
Normalized fluorescence intensity (A.U.)
distance (µm)
D
siControl
siAlix
siCHMP4C
% of NE buds with UIF signal
79%
21%
44%
56%
46%
54%
UIF in
UIF around
E
ConA/UIF
ConA-Alexa488
siControl
siCLCC1
2 µm
F
P = 0.0059
NE bud diameter (µm)
siControl
siCLCC1
G
siControl
siCLCC1
Frequency of events
NE buds diameter (µm)
H
UIF nuclear intensity
P < 0.0001
mean grey value fold change
siControl
siAlix
I
UIF nuclear intensity
P < 0.0001
mean grey value fold change
siControl
siCLCC1
J
RT-qPCR
nuclear mRNA fold change siAlix/siControl
Ttn
Neb
ActB
K
RT-qPCR
nuclear mRNA fold change siCLCC1/siControl
Ttn
Neb
Myh4
ActB

Figure 6. ESCRT-III and CLCC1 depletion disrupts cargo trafficking through NE buds

(**A**) Efficiency of Alix (left panel), CHMP4C (middle panel), and CLCC1 (right panel) siRNA depletion in myotubes (day 6 of differentiation) was verified by RT-qPCR (data are presented as fold change relative to siRNA control). RT-qPCR of Myosin heavy chain 4 (Myh4) shows no change in this transcript abundance following Alix or CHMP4C depletion. (**B**) Frequency of NE buds observed in Alix-, CHMP4C- (left panel) or CLCC1-depleted (right panel) and control myotubes. (**C**) Representative images of NE buds (marked with white arrowhead) labeled with ConA-Alexa488 (green) in Alix- or CHMP4C-depleted and control myotubes. Cells were immunostained with an antibody against endogenous UIF (magenta) to localize NEB cargoes. Graphs on the right represent the intensity profiles from the line scans indicated in the merge images (white dashed lines). (**D**) Quantification of percent of NE buds (from C) with UIF localized to the surface ('UIF around') or lumen ('UIF in') of the bud in Alix- and CHMP4C-depleted and control myotubes. (**E**) Representative images of CLCC1-depleted myotubes reveal enlarged NE buds labeled with ConA-Alexa488 (green; marked with white arrowheads). Cells were immunostained with an antibody against endogenous UIF (magenta) to localize NEB cargoes. (**F**) Quantification of NEB diameter (using ConA staining) in CLCC1-depleted and control myotubes from the experiment shown in (E). (**G**) Frequency distribution of NE bud size in CLCC1-depleted and control myotubes (n= 51 and 75 NE buds analyzed for siControl and siCLCC1, respectively). Frequency of events is represented as the fraction of NE buds in each binning range on the total of NE buds analyzed (equal to 1). Gaussian fits are represented in the graph. (**H-I**) Quantification of nuclear endogenous UIF fluorescence intensity in Alix-depleted (H) or CLCC1-depleted (I) versus siRNA control myotubes. Representative images are shown in Figure S4. (**J-K**) RT-qPCR analysis of mRNA extracted from fractionated nuclei from Alix-depleted (J) or CLCC1-depleted (K) versus siRNA control myotubes. Note that a nuclear increase is observed for Titin (Ttn) and Nebulin (Neb) transcripts (reported as fold change of Alix or CLCC1-depleted relative to control samples), relative to no nuclear increase for beta-Actin and Myh4 (used as control transcripts not found within NE buds). Mean and standard deviation are represented in each graph. All experiments were performed with n = 3 independent biological replicates. Scale bars are reported below every image.

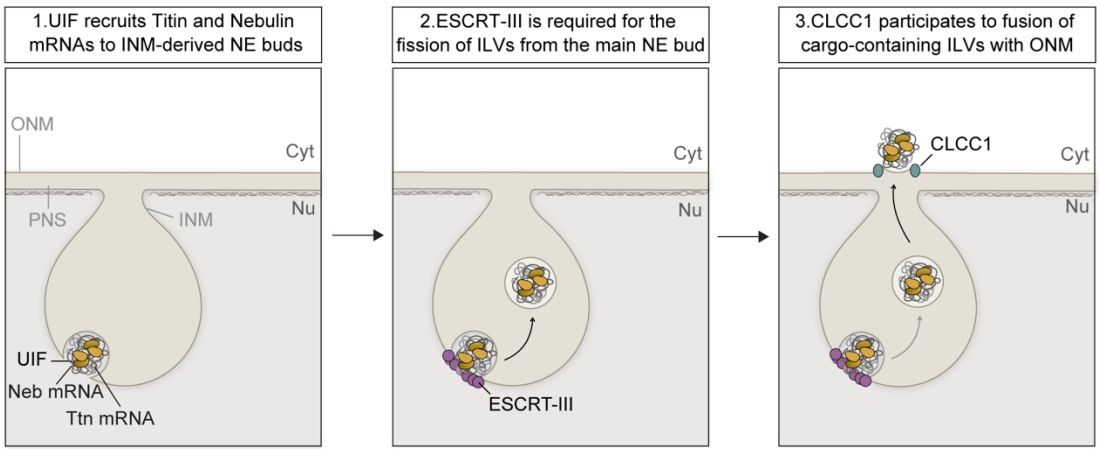

Figure 7. Molecular mechanism model for NEB-mediated export of large sarcomeric mRNAs